Low-temperature phase transition and magnetic properties of K3YbSi2O7

Predrag Dabić, Volker Kahlenberg, Biljana Krüger, Marko Rodić, Sabina Kovač, Jovan Blanuša, Zvonko Jagličić, Ljiljana Karanović, Václav Petříček, Aleksandar Kremenović

STRUCTURAL SCIENCE
CRYSTAL ENGINEERING
MATERIALS

ISSN: 2052-5206
journals.iucr.org/b

Low-temperature phase transition and magnetic properties of $K_3YbSi_2O_7$

Predrag Dabić, Volker Kahlenberg, Biljana Krüger, Marko Rodić, Sabina Kovač, Jovan Blanuša, Zvonko Jagličić, Ljiljana Karanović, Václav Petříček and Aleksandar Kremenović

Acta Cryst. (2021). B**77**, 584–593

STRUCTURAL SCIENCE CRYSTAL ENGINEERING MATERIALS

ISSN 2052-5206

Low-temperature phase transition and magnetic properties of $K_3YbSi_2O_7$

Predrag Dabić,[a]* Volker Kahlenberg,[b] Biljana Krüger,[b] Marko Rodić,[c] Sabina Kovač,[a] Jovan Blanuša,[d] Zvonko Jagličić,[e,f] Ljiljana Karanović,[a] Václav Petříček[g] and Aleksandar Kremenović[a]

[a]University of Belgrade, Faculty of Mining and Geology, Đušina 7, Belgrade, 11000, Serbia, [b]Institute of Mineralogy and Petrography, University of Innsbruck, Innrain 52, Innsbruck, A-6020, Austria, [c]Department of Chemistry, Biochemistry and Environmental Protection, Faculty of Sciences, University of Novi Sad, Trg Dositeja Obradovica 3, Novi Sad, 21000, Serbia, [d]University of Belgrade, Vinca Institute, Mike Petrovića Alasa 12-14, Belgrade, 11351, Serbia, [e]Faculty of Civil and Geodetic Engineering, University of Ljubljana, Jamova cesta 2, Ljubljana, 1000, Slovenia, [f]Institute of Mathematics, Physics and Mechanics, Jadranska 19, Ljubljana, 1000, Slovenia, and [g]Structure Analysis, Institute of Physics, Academy of Sciences of the Czech Republic, Na Slovance 1999/2, Praha 8, 18221, Czech Republic. *Correspondence e-mail: predrag.dabic@rgf.bg.ac.rs

Received 31 January 2021
Accepted 10 June 2021

Edited by P. Bordet, Institut Néel, France

Keywords: alkali rare-earth silicates; phase transition; magnetic properties; crystal field splitting; lanthanide silicates.

CCDC references: 1774871; 2089284

Supporting information: this article has supporting information at journals.iucr.org/b

The new ambient-temperature hexagonal (space group $P6_3/mmc$) polymorph of tripotassium ytterbium(III) disilicate (β-$K_3YbSi_2O_7$) has been synthesized by the high-temperature flux method and subsequently structurally characterized. In the course of the temperature-dependent single-crystal diffraction experiments, a phase transformation of β-$K_3YbSi_2O_7$ to a novel low-temperature orthorhombic phase (β'-$K_3YbSi_2O_7$, space group $Cmcm$) has been observed at about 210 K. β-$K_3YbSi_2O_7$ is isostructural with $K_3ErSi_2O_7$, whereas β'-$K_3YbSi_2O_7$ adopts a new type of structure. Both compounds can be built up from a regular alternation of layers of two types, which are parallel to the (001) plane. In the octahedral layer, YbO_6 octahedra are isolated and linked by $K1O_{6+3}$ polyhedra. The second, slightly thicker sorosilicate layer is formed by a combination of Si_2O_7 dimers and $K2O_{6+3}$ polyhedra. The boundary between the layers is a pseudo-kagome oxide sheet based on 3.6.3.6 meshes. The phase transition is due to a tilt of the two SiO_4 tetrahedra forming a single dimer which induces a decrease of the Si—O—Si angle between bridging Si—O bonds from 180° (dictated by symmetry in space group $P6_3/mmc$) to ≃164°. Magnetic characterization indicates that $K_3YbSi_2O_7$ remains paramagnetic down to 2 K, showing no apparent influence of the phase transformation on its magnetic properties. Analysis of the magnetization data revealed the positions of the three lowest crystal field levels of the Yb^{3+} cations, as well as the corresponding projections of their angular momentum on the direction of the magnetic field.

1. Introduction

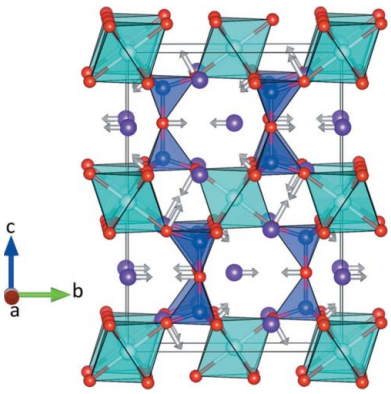

A wide range of optical and magnetic properties of rare-earth elements (REE), their alloys and compounds makes them very interesting materials for different applications. In recent decades, many studies have been performed on REE-bearing silicates (REE silicates) because they combine high thermal stability with interesting luminescent and magnetic properties (Felsche, 1973; Latshaw *et al.*, 2015*a*; Figueiredo *et al.*, 2016, and references cited therein).

REE silicates also exhibit a broad structural diversity (Liebau, 1985). According to their magnetic properties, the alkaline REE silicate structures can be roughly classified into three groups: paramagnetic structures (Latshaw *et al.*, 2015*b*; 2016*a*,*b*), structures which exhibit van Vleck paramagnetism (Latshaw *et al.*, 2015*b*,*c*,*a*; Morrison *et al.*, 2017) and structures

with antiferromagnetic ordering (Latshaw *et al.*, 2015*c*,*a*; Morrison *et al.*, 2017). In all reported samples, the zero-field cooled magnetic susceptibility was measured as a function of temperature between 2 and 300 K in an applied field of 1000 Oe. Latshaw *et al.* (2016*b*) reported the first study on the magnetism of the structural family of $Na_3REESi_2O_7$ compounds (REE = Ho, Yb), which are paramagnetic and similar in composition with respect to the $K_3YbSi_2O_7$ samples investigated in this contribution.

For several REE orthosilicates (REE_2SiO_5) and REE disilicates ($REE_2Si_2O_7$), polymorphic phase transitions between different modifications have been already reported (Sun *et al.*, 2014; Voronko *et al.*, 2015; Gao *et al.*, 2019; Hu *et al.*, 2019; among others). Actually, most of these phase transitions are reconstructive and occur at high temperatures (Felsche, 1973). However, there is also an example of a displacive phase transition, which was reported for Eu_2SiO_4 (Busch *et al.*, 1970; Funk *et al.*, 2018). Eu_2SiO_4 adopts monoclinic symmetry at room temperature and transforms to an orthorhombic structure at 438 K. Ananias and co-authors (2015) reported a low-temperature phase transition in $NaGd_{0.99}Eu_{0.01}SiO_4$. Its crystal structure was solved from single-crystal X-ray diffraction (SCXRD) data collected at 100 K and described in orthorhombic space group *Pnma*. Lowering the temperature resulted in a change to a body-centred phase with the *Imma* symmetry (measured at 30 K). Furthermore, a pressure-induced phase transition in REE silicates with the apatite-type structure [$REE_{4.67}(SiO_4)_3O$, hexagonal, $P6_3/m$] was reported recently (Zhang *et al.*, 2012, 2013). The application of high pressure causes a tilt of the isolated SiO_4 tetrahedra and triggers a symmetry reduction from $P6_3/m$ to $P6_3$. Notably, the pressure-induced phase transition in these apatite compounds is a reversible process.

For potassium-containing rare-earth disilicates two structure types have been described so far, which crystallize in the space groups $P6_3/mcm$ and $P6_3/mmc$, respectively (Vidican *et al.*, 2003; Latshaw *et al.*, 2016*c*; Dabić *et al.*, 2019). The crystal structure of α-$K_3YbSi_2O_7$ has been known for quite some time. It crystallizes in hexagonal space group $P6_3/mcm$ with the following unit-cell parameters: a = 9.78190 (10), c = 14.2401 (3) Å, V = 1180.02 (3) Å^3, Z = 6 (Vidican *et al.*, 2003). In this work we demonstrate that a second ambient-temperature modification of $K_3YbSi_2O_7$ with $P6_3/mmc$ symmetry can be prepared as well (β-$K_3YbSi_2O_7$). Crystal structures of these two ambient-temperature polymorphs consist of the same building units: Si_2O_7 groups and YbO_6 polyhedra which are connected into a three-dimensional framework with K^+ cations located in cavities in the net. In the crystal structure of α-$K_3YbSi_2O_7$, the Yb^{3+} cations are found both in octahedral and trigonal prismatic coordination, while Yb^{3+} cations in the crystal structure of β-$K_3YbSi_2O_7$ are octahedrally coordinated only. By lowering the temperature during a single-crystal diffraction experiment, β-$K_3YbSi_2O_7$ transformed into a low-temperature polymorph (β'-$K_3YbSi_2O_7$). The crystal structures of both modifications were determined. The magnetic properties of $K_3YbSi_2O_7$ are interpreted based on the features of its crystal structures. Using group theory, the structural phase transition between β- and β'-$K_3YbSi_2O_7$ was analyzed in more detail and its possible influence on the magnetic properties of $K_3YbSi_2O_7$ was examined.

2. Experimental

2.1. Synthesis and crystallization of $K_3YbSi_2O_7$

Single crystals were obtained during a high-temperature flux synthesis experiment using 0.0942 g of a nutrient consisting of a mixture of Yb_2O_3 (Sigma-Aldrich, 99.99%) and SiO_2 (Merck, p.a.) in the molar ratio of 1:12 and KF flux (2 g; Centrohem, 99%). After homogenization in an agate mortar, the material was transferred to a platinum crucible, covered with a lid and then placed in a furnace with resistance wire heating elements. Starting from room temperature the sample was heated to 1273 K with a rate of 200 K h^{-1}. The maximum temperature was maintained for 12 h. Subsequently, the container was cooled to 1023 K at a rate of 2 K h^{-1}. When reaching a temperature of 1023 K, the furnace was switched off. The resulting material was manually removed from the crucible, washed with distilled water and air-dried. Prismatic colourless single crystals up to 500 µm in size were observed, embedded in a polycrystalline matrix of KF.

2.2. Single-crystal X-ray diffraction measurement, structure solution and refinement

Single-crystal XRD data were collected for crystal 1 at ambient conditions (298 K) and at low temperature (100 K). A total of 21 datasets were acquired while cooling crystal 2 from ambient conditions to 93 K in steps of 10 K. The last measurement was performed on crystal 2 at ambient conditions after low-temperature treatment (Table 1). Single crystals were fixed on glass fibres using nail polish as glue. An analytical absorption correction based on indexed crystal faces using the procedure of Clark & Reid (1995) in combination with an empirical absorption correction using spherical harmonics (implemented in SCALE3 ABSPACK scaling algorithm) were applied during the data reduction. All structures were refined on F^2 by full-matrix least-squares techniques using the programs *SHELXL* (Sheldrick, 2015) and *Jana2006* (Petříček *et al.*, 2014).

The structure of the ambient-temperature polymorph of $K_3YbSi_2O_7$ (datablock beta-$K_3YbSi_2O_7$ in the CIF) crystallizes in space group $P6_3/mmc$. It is isostructural with $K_3ErSi_2O_7$ (Dabić *et al.*, 2019). Therefore, atomic coordinates of this structural analogue were used as a starting model for structure refinement, where Er was replaced with Yb. The crystal structure was refined to R = 0.013. The structure of the $K_3YbSi_2O_7$ crystal studied at 100 K (datablock beta_prime-$K_3YbSi_2O_7$ in the CIF) showed lower Laue symmetry (*mmm*) and systematic absences in agreement with space group *Cmcm*. The structure of the low-temperature modification was solved using the program *SUPERFLIP* (Palatinus & Chapuis, 2007) and refined to R = 0.027. The structures of the crystal at ambient conditions ($P6_3/mmc$) and at 100 K (*Cmcm*) differ

Table 1
Selected crystals for XRD measurements and temperatures of data collections.

	Crystal 1	Crystal 2	Polymorph
T (K)	298	293, 283, ..., 213 295†	β-$K_3YbSi_2O_7$ (space group $P6_3/mmc$)
	100	203, 193, ..., 93	β'-$K_3YbSi_2O_7$ (space group $Cmcm$)

† Repeated data collection for crystal 2 after the low-temperature study.

from the known hexagonal polymorph of α-$K_3YbSi_2O_7$ reported in $P6_3/mcm$ by Vidican *et al.* (2003). The structures corresponding to the nine data sets collected between ambient conditions and 213 K were refined using the hexagonal model in $P6_3/mmc$. The 12 structures studied between 203 and 93 K were refined using the orthorhombic model (space group $Cmcm$).

For β'-$K_3YbSi_2O_7$, pseudo-merohedral threefold twinning was observed for all temperatures. Three possible C-centred orthohexagonal settings showed similar internal residuals with values of $R_{int} \simeq 0.035$–0.045, indicating the presence of three twin-domains forming a so-called drilling. Data were indexed and processed using the setting of one of the domains. The crystal structure was solved in space group $Cmcm$. Using the TWIN [0.5 0.5 0.0 −1.5 −0.5 0.0 0.0 0.0 1.0 3] and BASF [0.33 0.33] instructions of *SHELXL* all three C-centred domains were included in the refinement. A similar type of twinning was noticed in $CsLiSO_4$ (Petříček *et al.*, 2016), for example. The orthorhombic phase exhibits a pronounced hexagonal pseudo-symmetry (Giacovazzo *et al.*, 1992) corresponding to the parent β-phase of symmetry $P6_3/mmc$. The effect of pseudo-symmetry was quite pronounced for β'-$K_3YbSi_2O_7$, causing unstable refinements of some anisotropic atomic displacement parameters. Therefore, in some cases it was necessary to constrain them according to the restrictions of the higher symmetrical second-rank tensor of the hexagonal structure (Peterse & Palm, 1966) (for details, see CIF file within the supporting information). Furthermore, the twinning itself lead to significant problems when refining atomic displacement parameters in highly absorbing compounds due to the so-called screening effect (Petříček *et al.*, 2016). However, even in the hexagonal β-structure the refinement of the displacement parameters of the oxygen atoms was not always straightforward due to pseudo-symmetry effects. For example, the change of the U_{33} component of atom O2 significantly influences the calculated structure factors associated with reflections in the $hk7$, $hk11$, and $hk15$ layers. Given that reflections in the hkl layers where l is odd are very weak – a direct consequence of the pseudo-symmetry of the hexagonal crystal structure – the low accuracy of their measured intensities may be the reason for the problems when refining the atomic displacement parameters of O2 anisotropically in the hexagonal polymorph. Similar effects concerning the influence of pseudo-symmetry on atomic displacement parameters were noticed in $Ba_3Al_2O_6$ (Lazic *et al.*, 2009). Details about the crystal structures of β-$K_3YbSi_2O_7$ and β'-$K_3YbSi_2O_7$, the phase transition and the observed twinning are presented in Sections 3.1 and 3.2. The most relevant information about data collections and refinements is compiled in Table 2. Selected bond lengths, bond angles and

Table 2
Experimental details.

Experiments were carried out with Mo $K\alpha$ radiation using a Rigaku Oxford Diffraction Gemini Ultra diffractometer. An analytical absorption correction based on indexed crystal faces using the procedure of Clark & Reid (1995) in combination with an empirical absorption correction using spherical harmonics (implemented in SCALE3 ABSPACK scaling algorithm) were applied.

	β-$K_3YbSi_2O_7$	β'-$K_3YbSi_2O_7$
Crystal data		
Chemical formula	$K_3O_7Si_2Yb$	$K_3O_7Si_2Yb$
M_r	458.52	458.5
Crystal system, space group	Hexagonal, $P6_3/mmc$	Orthorhombic, $Cmcm$
Temperature (K)	298	100
a, b, c (Å)	5.7274 (5), 5.7274 (5), 13.9339 (15)	5.7099 (5), 9.8898 (9), 13.8867 (14)
α, β, γ (°)	90, 90, 120	90, 90, 90
V (Å^3)	395.84 (8)	784.18 (13)
Z	2	4
μ (mm^{-1})	13.69	13.82
Crystal size (mm)	0.28 × 0.09 × 0.08	0.28 × 0.09 × 0.08
Data collection		
T_{min}, T_{max}	0.110, 0.450	0.107, 0.444
No. of measured, independent and observed reflections	2409, 208, 187 [$I > 2\sigma(I)$]	2644, 922, 840 [$I > 2\sigma(I)$]
R_{int}	0.040	0.045
$(\sin\theta/\lambda)_{max}$ (Å^{-1})	0.649	0.704
Refinement		
$R[F^2 > 2\sigma(F^2)]$, $wR(F^2)$, S	0.013, 0.035, 1.17	0.027, 0.064, 1.14
No. of reflections	208	922
No. of parameters	20	26
$\Delta\rho_{max}$, $\Delta\rho_{min}$ (e Å^{-3})	1.02, −0.44	1.40, −0.77

Computer programs: *CrysAlisPro* 1.171.38.43 (Rigaku Oxford Diffraction, 2014), *SUPERFLIP* (Palatinus & Chapuis, 2007), *SHELXL2018/3* (Sheldrick, 2015), *Jana2006* (Petříček *et al.*, 2014), *VESTA* (Momma & Izumi, 2011).

Table 3
Selected bond lengths (Å) and angles (°) for β-$K_3YbSi_2O_7$.

K1—O1	2.8668 (3) ×6	Yb1—O1^{ii}	2.220 (2) ×5
K1—O1^{i}	3.032 (3) ×3	Yb1—O1	2.221 (2)
K2—O1	2.785 (3) ×6	Si1—O1	1.615 (2) ×3
K2—O2	3.3067 (3) ×3	Si1—O2	1.6411 (17)
O1—Si1—O1^{iii}	110.65 (11) ×3	Si1^{iv}—O2—Si1	180.0
O1—Si1—O2	108.27 (11) ×3		

Symmetry code: (i) $x-y, x, -z$; (ii) $-y, x-y, z$; (iii) $-x+y+1, -x+1, z$; (iv) $x, y, -z+\frac{1}{2}$.

Table 4
Bond valence sums v_{ij} (v.u.) for the cations and anions in β-polymorph.

	K1^a	K2^a	Yb^a	Si^b	Σv_{ij} (v.u.)
O1	0.137 × 6 0.088 × 3	0.171 × 6	0.502 × 5 0.501	1.025 × 3	2.06
O2		0.042 × 3		0.955	2.036
Σv_{ij} (v.u.)	1.086	1.152	3.011	4.03	

References for bond valence parameters: (*a*) Brown & Altermatt (1985), (*b*) Brese & O'Keeffe (1991).

the results of bond-valence-sum calculations [*VaList* software, Wills, 2010; bond valence parameters: Brown & Altermatt (1985) and Brese & O'Keeffe (1991)], are presented in Tables 3, 4, 5 and 6. Drawings of the crystal structures were prepared using the program *VESTA* (Momma & Izumi, 2011).

2.3. Magnetic measurements (SQUID magnetometry)

The magnetic properties of $K_3YbSi_2O_7$ were investigated using a Quantum Design MPMS-XL-5 susceptometer equipped with a SQUID sensor. The temperature dependencies of the magnetic susceptibilities were measured over the temperature range 2–300 K. The measurements of the magnetic properties were performed on a sufficiently large single crystal (Fig. S4). The selected single crystal, which gave a reliable magnetic signal, was oriented such that the direction of the crystallographic *c* axis was perpendicular to the external magnetic field. The mass of the selected single crystal (96 µg) was calculated indirectly from the crystal volume obtained by describing the crystal morphology using crystal faces.

3. Results and discussion

3.1. Single-crystal X-ray diffraction and description of the structures

As representatives for the description of β- and β'-$K_3YbSi_2O_7$, the structures determined from the data collections for crystal 1 at 298 and 100 K were used, respectively. Both polymorphs can be described as a three-dimensional framework made up of Si_2O_7 groups and YbO_6 octahedra with large potassium ions located in cavities of the network. The potassium atoms occupy two different crystallographic positions and in both sites they are nine-coordinated by oxygen atoms. Alternatively, the structures can be described as formed by a regular alternation of two types of layers, which

Table 5
Selected bond lengths (Å) and angles (°) for β'-$K_3YbSi_2O_7$.

K1—O1	2.842 (5) ×2	K2—O3^{iii}	2.938 (10)
K1—O1^{i}	2.876 (5) ×2	K2—O3^{iv}	3.489 (6) ×2
K1—O1^{ii}	3.144 (4) ×2	Si1—O1^{v}	1.623 (5) ×2
K1—O2^{i}	2.833 (7)	Si1—O2	1.609 (7)
K1—O2^{ii}	2.8600 (6) ×2	Si1—O3	1.651 (2)
K2—O1	2.742 (4) ×4	Yb1—O1	2.212 (4) ×4
K2—O2^{iii}	2.827 (7) ×2	Yb1—O2	2.222 (6) ×2
O1^{v}—Si1—O1^{vi}	111.0 (3)	O2—Si1—O3	105.3 (4)
O1^{v}—Si1—O2	110.8 (2) ×2	Si1—O3—Si1^{vii}	164.3 (7)
O1^{v}—Si1—O3	109.4 (2) ×2		

Symmetry codes: (i) $x+\frac{1}{2}, y+\frac{1}{2}, z$; (ii) $x, -y, -z+1$; (iii) $-x, -y, z-\frac{1}{2}$; (iv) $-x-\frac{1}{2}, -y-\frac{1}{2}, z-\frac{1}{2}$; (v) $x-\frac{1}{2}, -y-\frac{1}{2}, -z+1$; (vi) $-x+\frac{1}{2}, -y-\frac{1}{2}, -z+1$; (vii) $-x, y, -z+\frac{3}{2}$.

Table 6
Bond valences v_{ij} (v. u.) for polymorph β'-$K_3YbSi_2O_7$.

	K1^a	K2^a	Yb^a	Si^b	Σv_{ij} (v. u.)
O1	0.147 × 2 0.134 × 2 0.065 × 2	0.192 × 4	0.513 × 4	1.003 × 2	2.054
O2	0.15 0.14 × 2	0.153 × 2	0.499 × 2	1.041	2.123
O3		0.113 0.026 × 2		0.930	2.025
Σv_{ij} (v. u.)	1.122	1.239	3.05	3.977	

References for bond valence parameters: (*a*) Brown & Altermatt (1985), (*b*) Brese & O'Keeffe (1991).

are parallel to (001): (1) octahedral layers, that are formed of YbO_6 octahedra and $K1O_{6+3}$ coordination polyhedra, and (2) sorosilicate layers, which contain Si_2O_7 dimers interconnected by tricapped trigonal $K2O_{6+3}$ prisms. The octahedral layer is thinner (its width is about 2.7 Å along [001]) and is located at $z \simeq 0$. The alternating sorosilicate slab situated at $z \simeq \frac{1}{4}$ is significantly thicker (thickness: ∼4.3 Å). By sharing common vertices each YbO_6 octahedron from the octahedral layer is linked to six Si_2O_7 groups from two neighbouring sorosilicate slabs *via* Yb–O–Si linkages.

At the boundary between adjacent octahedral and sorosilicate layers, oxygen sheets with 3.6.3.6 meshes formed by terminal nonbridging O atoms can be identified [Figs. 1(*a*) and 1(*b*)]. These common O atoms form a pseudo-kagome pattern composed of triangles and hexagons (O'Keeffe & Hyde, 1996). Unlike a regular kagome pattern, however, smaller and larger triangles can be distinguished which surround the central six-membered ring [Figs. 1(*c*) and 1(*d*)]. The O···O distances in the smaller equilateral triangles are ≃ 2.66 Å, whereas in the larger ones values of ≃ 3.06 Å are observed. The symmetry of a single oxygen sheet is trigonal. Figs. 1(*c*) and 1(*d*) show a comparison between the pseudo-kagome patterns of the O1 atoms in β-$K_3YbSi_2O_7$ *versus* a pattern obtained in the equivalent sheet of the O1 and O2 atoms in β'-$K_3YbSi_2O_7$.

3.1.1. Crystal structure of β-$K_3YbSi_2O_7$. In the hexagonal β-$K_3YbSi_2O_7$ structure, Yb^{3+} cations are octahedrally coordinated with uniform Yb—O distances of 2.220 (2) Å, which is

close to the value of 2.268 Å (0.868 Å + 1.4 Å) calculated from the ionic radii (Shannon, 1976). The shortest distance between two Yb sites (~5.7 Å = *a*) is close to the sum 5.6 Å of van der Waals radii (Alvarez, 2013). The YbO_6 octahedra are connected by $K1O_{6+3}$ coordination polyhedra forming the so-called octahedral layer (Figs. 1 and 2).

The coordination polyhedron about the potassium cations $K1^+$ can be described as a non-distorted hexagonal pyramid with a triple vertex, or as a truncated hexagonal pyramid with a regular hexagonal base upon which a parallel triangular face is situated [Figs. 1(*a*) and 2(*a*)]. This parallel triangular face (small equilateral triangle in the oxygen sheet with the 3.6.3.6 meshes) is a common triangular face with SiO_4 tetrahedra from the adjacent sorosilicate Si_2O_7 group. Six equal K1–O1 bonds of 2.8668 (3) Å are formed with the basal oxygen atoms. These bonds are slightly longer than the sum of ionic radii 2.78 Å (1.38 Å + 1.4 Å) for K^+ cation with CN = 6 (Shannon, 1976). Additional three K1—O1 bonds of 3.032 (3) Å formed with the three oxygen atoms positioned in the upper triangular face, are slightly longer. These three K1—O1 bonds are longer than the sum of the ionic radii 2.95 Å (1.55 Å + 1.4 Å) for K^+ cation with CN = 9. The K1 cation is not positioned near the centre of the 6+3 coordination polyhedron, but it is significantly shifted towards the basal plane and resides in the centre of a basal hexagon. Taking into account the nine nearest neighbouring O1 atoms, the bond valence sum of 1.086 v.u. around the K1 is very close to its valence state of +1 (Table 4).

The Si_2O_7 groups represent isolated units formed by two SiO_4 tetrahedra which share one vertex [Figs. 3(*a*) and 3(*c*)]. They are parallel to the *c* axis with an Si—O—Si angle of 180°, which is dictated by the symmetry of space group $P6_3/mmc$ and a comparatively rare structural feature in silicate structures (Liebau, 1985). The Si—O distances in the SiO_4 tetrahedra are shorter than the calculated value of 1.66 Å (0.26 Å + 1.4 Å) from the ionic radii (Shannon, 1976). As can be expected, the bridging Si—O2 bond of 1.6411 (17) Å is longer than the three nonbridging Si—O1 bonds of 1.615 (2) Å. The tetrahedral O—Si—O bond angles of 108.27 (11)° and 110.65 (11)° are rather typical for oxo-silicates (Liebau, 1985) and close to the ideal tetrahedral angle of 109.5°. The bridging Si—O bonds are in agreement with the results of the statistical analysis given by O'Keefe and Hyde (1978). These authors found an empirical relationship between the Si—O bond distance *l*, the Si—O—Si angle θ and the non-bonded Si···Si distance *d*: $l = (d/2)/\sin(\theta/2)$. The predicted Si—O bond length *l* is 1.641 Å [for the Si—O—Si angles of 180° and a Si···Si distance of 3.282 (3) Å], which compares well with the experimentally determined Si—O_{br} distance.

Considering bond distances up to 3 Å, the potassium cations K2 have sixfold coordination with six equal K2—O1 distances of 2.785 (3) Å. The shape of the coordination polyhedron is a regular trigonal prism [Figs. 1(*e*), 3(*a*) and 3(*c*)].

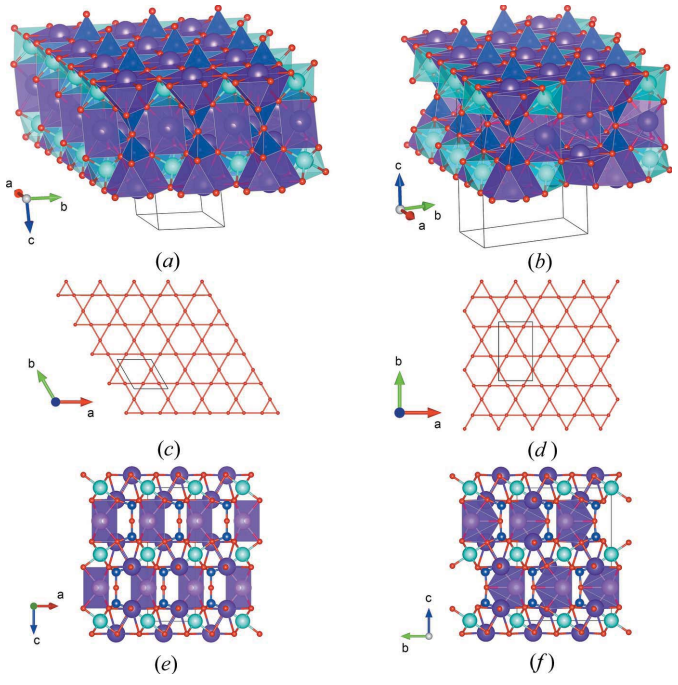

Figure 1
Sequence of alternating octahedral and sorosilicate layers in (*a*) hexagonal β-$K_3YbSi_2O_7$ and (*b*) orthorhombic β'-$K_3YbSi_2O_7$. The pseudo-kagome pattern 3.6.3.6 produced by the terminal O atoms in (*c*) hexagonal structure of β-$K_3YbSi_2O_7$ and (*d*) orthorhombic structure of β'-$K_3YbSi_2O_7$. Trigonal $K2O_6$ prisms (*e*) and monocapped trigonal $K2O_{6+1}$ prisms (*f*) form sorosilicate layers sharing common vertices and edges with the Si_2O_7 groups, respectively. Atoms are shown as spheres using the following colour code: Yb: turquoise, Si: blue, K: violet, O: red.

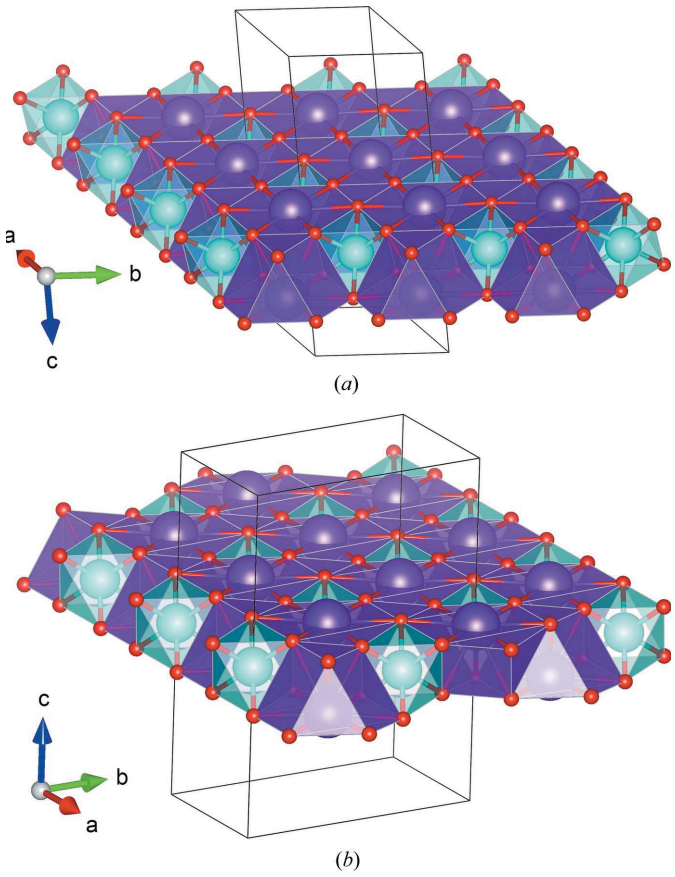

Figure 2
Isolated YbO_6 octahedra and $K1O_{6+3}$ coordination polyhedra in (*a*) a single flat octahedral layer in β-$K_3YbSi_2O_7$ and (*b*) a slightly corrugated octahedral layer in β'-$K_3YbSi_2O_7$. The colour coding is as in Fig. 1.

The triangular basal face (corresponding to the large equilateral triangle in the oxygen sheet with the 3.6.3.6 meshes) corresponds to an octahedral face of a YbO_6 octahedron from the adjacent octahedral layer. Taking three additional longer K2—O2 bonds of 3.3067 (3) Å into account, the coordination polyhedron around K2 can be described as a tricapped trigonal prism, $K2O_{6+3}$. The calculated bond valence sum is 1.152 v.u., indicating that K2 is slightly overbonded when considering all nine neighbouring O atoms, while it is around 1.0 v.u. for the closest six O atoms only (Table 4). In the sorosilicate layers, each Si_2O_7 group is linked to three tricapped trigonal $K2O_6$ prisms by sharing common edges. Furthermore, each dimer is connected to six different Yb^{3+} cations of the octahedral layers by sharing common corners.

3.1.2. Crystal structure of β'-$K_3YbSi_2O_7$. The orthorhombic *Cmcm* structure of β'-$K_3YbSi_2O_7$ is only slightly different from the hexagonal $P6_3/mmc$ model. It possesses an almost ideal orthohexagonal unit cell with an a/b ratio of $3^{1/2}$. The asymmetric unit contains two potassium, one ytterbium, one silicon and three unique oxygen sites. The structural phase transition is characterized by small shifts of the atomic positions and minor changes in the coordination environments of the potassium ions.

The Yb^{3+} cations are octahedrally coordinated with four oxygen atoms at Yb–O1 distances of 2.212 (4) Å and two oxygen atoms at Yb–O2 distances of 2.222 (6) Å. The average Yb—O distance, ⟨2.2153 Å⟩, is almost identical to the value of 2.220 (2) Å found in the hexagonal β-$K_3YbSi_2O_7$ polymorph. Both O1 and O2 oxygen atoms are further linked to one silicon and four potassium atoms (three K1 and one K2). In agreement with the hexagonal β-$K_3YbSi_2O_7$ polymorph, the coordination polyhedron of K1 in β'-$K_3YbSi_2O_7$ can also be described as a truncated hexagonal pyramid containing two parallel faces: a hexagonal base and a parallel triangular face at the top. K1 is located in the centre of a regular O_6 hexagon formed by four O1 and two O2 atoms. The six K1—O bonds with the six O atoms in the hexagonal base range from 2.833 (7) to 2.876 (5) Å. The bond length calculated from the ionic radii of 2.78 Å (for K cation with CN = 6) is slightly smaller than the experimental values. The shortest and the longest two K1—O bonds [K1—O2 = 2.833 (7) Å and two K1—O1 = 3.144 (4) Å, respectively] are formed with O atoms situated at the vertices of the upper triangular face. The coordination polyhedron about K1 is completed by three bridging O3 atoms located below the hexagonal base showing very long contacts (K1—O3 is about 3.9 Å). Considering only the 6 + 3 shorter bonds the bond valence sum of 1.122 v.u. for K1 is close to its valence state +1 (Table 6).

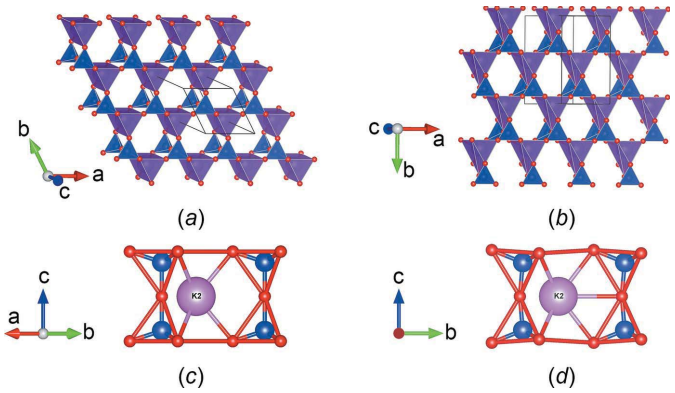

Figure 3
Trigonal prismatic $K2O_6$ coordination polyhedra and tetrahedra of the Si_2O_7 groups in β-$K_3YbSi_2O_7$. Bridging O atoms define an Si—O—Si angle of 180° (*a*, *c*). β'-$K_3YbSi_2O_7$: monocapped trigonal prismatic $K2O_{6+1}$ coordination polyhedra are formed as a result of a coupled tilting of the tetrahedra in the Si_2O_7 groups. Consequently, the bridging O atoms are shifted and form a Si—O—Si angle less than 180° (*b*, *d*). The colour coding is as in Fig. 1.

The phase transition involves a coupled tilting of the tetrahedra in the Si_2O_7 groups in which bridging O atoms shift and form Si—O—Si angle less than 180°. In the β'-$K_3YbSi_2O_7$ structure, the Si—O—Si angle has a value of 164.3 (7)° at 100 K, which is significantly smaller than the analogous angle of 180° in the β-$K_3YbSi_2O_7$ structure. According to quantum-mechanical calculations (Meagher *et al.*, 1979; Gibbs *et al.*, 1981) Si—O—Si angles deviating from 180° are energetically more favourable. The bond distance from silicon to the bridging oxygen ion [1.651 (2) Å] is longer than the nonbridging Si—O bonds (1.609 (7) and 1.623 (5) Å). The tetrahedral O—Si—O bond angles range from 105.3 (4) to 111.0 (3)° showing a slightly larger deviation from the ideal tetrahedral angle of 109.5°. Using the empirical relationship $l = (d/2)/\sin(\theta/2)$ given by O'Keefe and Hyde (1978), the calculated Si—O bond length l is 1.651 Å for the Si—O—Si angle of 164.3 (7)° and Si···Si distance of 3.271 (3) Å, which is in excellent agreement with the experimentally obtained value of 1.651 (2) Å.

In comparison with the ideal trigonal-prismatic coordination polyhedron of K2 in the hexagonal polymorph, in the orthorhombic structure a slightly distorted monocapped trigonal prism is observed [Figs. 1(*f*), 3(*b*) and 3(*d*)]. Seven K2—O distances range between 2.742 (4) and 2.938 (10) Å: four shorter K2—O1 bonds with distances of 2.742 (4) Å, two longer K2—O2 bonds at 2.827 (7) Å and one long K2—O3 bond of 2.938 (10) Å. Including two additional quite long K2—O bonds [3.489 (6) Å] the coordination polyhedron becomes a rather distorted tricapped trigonal prism. The bond valence sums for the K2 atom in $K2O_6$ and in $K2O_{6+1}$ environments are 1.07 and 1.19 v.u., respectively (Table 6).

The coordination octahedra around Yb and the Si_2O_7 dimers are connected in the same way as in β-$K_3YbSi_2O_7$: each YbO_6 octahedron is linked to six different Si_2O_7 groups by corner sharing, while each Si_2O_7 group is connected to six different Yb^{3+} cations.

The temperature dependence of the unit-cell parameters and selected structural parameters are presented in the supplementary figures S1–S3. The plot of the unit-cell parameters as a function of temperature shows a more pronounced change of the *c* parameter with respect to *a* (Fig. S1). Near the critical temperature of the phase transition, the bridging oxygen angle Si—O—Si starts to decrease from 180° (dictated by space group symmetry of $P6_3/mmc$) to approximately 164° at 100 K (Fig. S2). The variations of the Yb—O bond distances as a function of temperature in β-$K_3YbSi_2O_7$ and β'-$K_3YbSi_2O_7$ are rather small (Fig. S3).

Table 7
The calculated reference structure for the aristotype hexagonal structure β-$K_3YbSi_2O_7$ in space group *Cmcm* (a = 5.7274 Å, b = 9.9201 Å, c = 13.9339 Å).

Atom	Wyckoff site		x	y	z
Yb1	4*a*	(0,0,0)	0	0	0.5
K1	8*f*	(0,*y*,*z*)	0.5	0.83333	0.5918
Si1	8*f*	(0,*y*,*z*)	0.5	0.16667	0.6322
K2	4*c*	(0,*y*,$\frac{1}{4}$)	0	0	0.75
O1	16*h*	(*x*,*y*,*z*)	0.7318	0.0894	0.5959
O1_2	8*f*	(0,*y*,*z*)	0.5	0.3212	0.5959
O2	4*c*	(0,*y*,$\frac{1}{4}$)	0.5	0.16667	0.75

Table 8
The displacement field for the low-temperature β'-$K_3YbSi_2O_7$ phase.

The values of u_x, u_y and u_z are given in relative units, while $|u|$ is the absolute displacement in Å.

Wyckoff site		Atom	u_x	u_y	u_z	$\|u\|$
4*a*	(0,0,0)	Yb1	0	0	0	0
8*f*	(0,*y*,*z*)	K1	0	−0.0072	0.0007	0.0725
8*f*	(0,*y*,*z*)	Si1	0	−0.0052	0	0.0513
4*c*	(0,*y*,$\frac{1}{4}$)	K2	0	−0.0185	0	0.1835
16*h*	(*x*,*y*,*z*)	O1	0.0024	−0.0100	0.0052	0.1263
8*f*	(0,*y*,*z*)	O1_2	0	−0.0101	−0.0093	0.1638
4*c*	(0,*y*,$\frac{1}{4}$)	O2	0	0.0177	0	0.1759

3.2. Symmetry relationships between two $K_3YbSi_2O_7$ polymorphs

Considering group theory, the structures of our two polymorphs of $K_3YbSi_2O_7$ are in a crystallographic group–subgroup relationship: the low-temperature-induced transition results in a maximal *translationengleiche* subgroup of index three. The relation between the basis vectors of the crystal structures belonging to space groups $G = P6_3/mmc$ and $H = Cmcm$ (subgroup) can be described by the following equations: $\mathbf{a}_{or} = -(\mathbf{a}_{hex} + \mathbf{b}_{hex})$; $\mathbf{b}_{or} = (\boldsymbol{a}_{\mathbf{hex}} - \mathbf{b}_{\mathbf{hex}})$; $\boldsymbol{c}_{\mathbf{or}} = \boldsymbol{c}_{\mathbf{hex}}$ (reverse transformation: $\mathbf{a}_{hex} = -(\frac{1}{2})(\mathbf{a}_{or} - \mathbf{b}_{or})$; $\mathbf{b}_{hex} = -(\frac{1}{2})(\mathbf{a}_{or} + \mathbf{b}_{or})$; $\mathbf{c}_{hex} = \mathbf{c}_{or}$). Actually, there are two other *Cmcm* subgroups (H' and H'') that belong to the same conjugacy class (H': $\mathbf{a}_{or} = \mathbf{a}_{hex}$; $\mathbf{b}_{or} = \mathbf{a}_{hex} + 2\mathbf{b}_{hex}$; $\mathbf{c}_{or} = \mathbf{c}_{hex}$ and H'': $\mathbf{a}_{or} = \mathbf{b}_{hex}$; $\mathbf{b}_{or} = -(2\mathbf{a}_{hex} + \mathbf{b}_{hex})$; $\mathbf{c}_{or} = \mathbf{c}_{hex}$). The crystal patterns associated with these three different domain states are energetically equivalent. Consequently, the crystal of the low-temperature modification should display threefold twinning ('drilling') about the *c* axis – a feature that was observed in the diffraction experiments. Furthermore, for the given origin choices in both modifications an additional origin shift of (0,0,$\frac{1}{2}$) has to be applied to map the two structures onto each other. In summary, one can say that the atomic coordinates of the high- and low-temperature structures of crystal 1 determined at 298 K and 100 K, respectively, are related by the following 4 by 4 transformation matrix:

$$\begin{pmatrix} -1 & 1 & 0 & 0 \\ -1 & -1 & 0 & 0 \\ 0 & 0 & 1 & \frac{1}{2} \\ 0 & 0 & 0 & 1 \end{pmatrix}$$

A more detailed understanding of the phase transformation in $K_3YbSi_2O_7$ can be achieved by symmetry-mode analysis. In the course of this procedure implemented in the program AMPLIMODES (Orobengoa *et al.*, 2009) the structural distortions present in the low-symmetry structure were decomposed into contributions from different modes, whose symmetries are given by the irreducible representations (irreps) of the space group of the parent (high symmetry) phase, *i.e.* the aristotype hexagonal structure (in the present case).

Due to the maximal group–subgroup relationship, the onset of one primary mode could already explain the observed symmetry break directly. It corresponds to the irreducible representation Γ_5^+ of space group $P6_3/mmc$ and is associated with the centre (0,0,0) of the first Brillouin zone. Therefore, the β'-$K_3YbSi_2O_7$ can be classified as properly ferroelastic. Furthermore, there can be also a trivial fully symmetrical Γ_1^+ distortion that retains the symmetry of β'-$K_3YbSi_2O_7$.

Using the input data mentioned above, a reference structure was calculated in a first step corresponding to the parent phase expressed in the setting of the low-symmetry phase (Table 7). Notably, a Wyckoff splitting can be observed. The oxygen position O1 (Wyckoff site 12*k* in $P6_3/mmc$) is split into two positions in *Cmcm*: O1 (16*h*) and O1_2 (8*f*), respectively. The resulting displacement field obtained from the comparison of the reference structure of β-$K_3YbSi_2O_7$ with the low-symmetry β'-$K_3YbSi_2O_7$ phase is given in Table 8. The displacement vectors **u** for the atoms in the asymmetric unit of the reference structure listed in this table completely define the displacive distortions relating both structures.

In the next step of mode analyses, a basis of symmetry-adapted modes for describing the displacive distortion was obtained performing the mode decomposition of the distortion based on it. A summary of the calculated distortion amplitudes is given in Table 9. It lists the two irreducible representations present in the distortion and the absolute amplitudes of these two symmetry components of the global distortion (last column). As can be seen from the amplitudes, the Γ_5^+ mode is significantly larger and could be almost exclusively used for a complete understanding of the distortion pattern. Furthermore, for each representation the table gives its wavevector, the order parameter direction in representation space that the modes fulfil, the resulting isotropy subgroup and the dimensions of its subspace. This dimension corresponds to the number of independent basis symmetry-adapted modes related to the specific irreducible representations. These numbers are 4 (for Γ_1^+) and 7 (for Γ_5^+). Therefore, a total number of 11 modes (parameters) are necessary to characterize the symmetry-breaking distortion, in accordance with the number of free positional parameters in the conventional description of the *Cmcm* structure (Table 8).

Finally, for each involved irreducible representation the corresponding polarization vector was obtained. Table 10 shows a crystallographic description of these normalized vectors. For the asymmetric unit of the reference structure for each involved irreducible representation, the set of correlated

Table 9
Summary of the mode decomposition of the low-temperature β'-$K_3YbSi_2O_7$ phase.

Wavevector	Irrep	Direction	Subgroup	Dimension	Amplitude (Å)
(0,0,0)	Γ_1^+	(*a*)	$P6_3/mmc$	4	0.0375
(0,0,0)	Γ_5^+	(−0.500*a*, −0.866*a*)	*Cmcm*	7	0.6236

atomic displacements (in relative units) is given. The actual distortion of a specific symmetry can be easily obtained by multiplying the components of the polarization vector with the amplitude summarized in Table 9. For Γ_5^+, for example, columns 5 to 7 have to be multiplied with the amplitude of 0.6236 Å.

From inspection of Table 10, it is clear that neither Γ_5^+ nor Γ_1^+ induces any displacements of the octahedrally coordinated Yb atoms. The symmetry breaking Γ_5^+ mode involves an in-phase movement of the two independent K atoms (though the amplitudes differ by a factor of about three) and an anti-phase displacement of the oxygen anion O2 along [010]. Notably, this specific shift leads to a deviation of the Si—O2—Si angle away from 180°. The Γ_5^+-triggered movements of O1_2 are located in the *yz* plane, whereas O1 has displacement components along all three directions. However, again, the largest contribution is parallel to the *b* axis. In order to obtain a better understanding of the distortion fields, individual displacements calculated for the dominant Γ_5^+ representation have been visualized using the program *VESTA* (Momma & Izumi, 2011) and are given in Fig. 4.

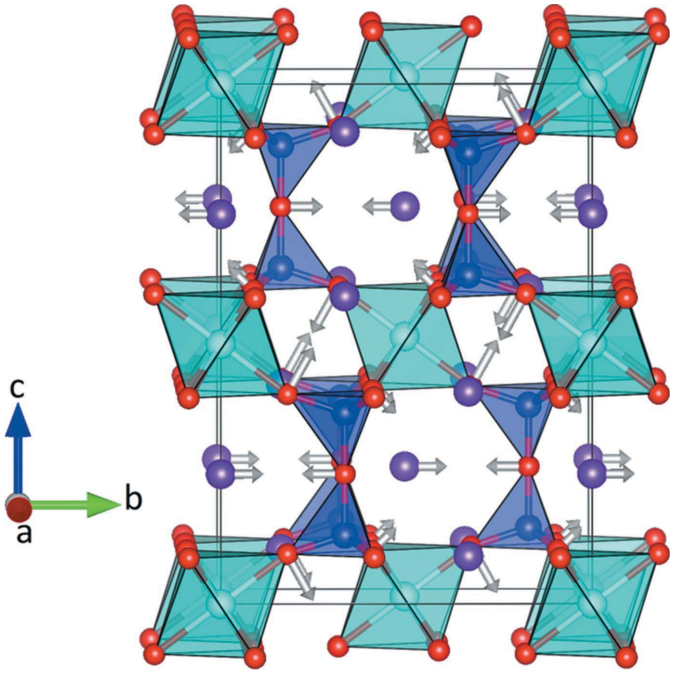

Figure 4
Displacement field induced by the irreducible representation Γ_5^+ on the atoms of the reference structure. For the sake of clarity, the magnitudes of individual shift vectors (grey) have been doubled. The colour coding is as in Fig. 1.

Table 10
Normalized polarization vectors of the Γ_1^+ and Γ_5^+ distortions present in the β'-$K_3YbSi_2O_7$ expressed as displacements (in relative units) of the atoms in the asymmetric unit of the reference structure (normalization unit: 1 Å).

	Γ_1^+			Γ_5^+		
Atom	δx	δy	δz	δx	δy	δz
Yb1	0	0	0	0	0	0
K1	0	0	0.0192	0	−0.0116	0
K2	0	0	0	0	−0.0297	0
Si1	0	0	0	0	−0.0083	0
O1	0.0306	−0.0102	0.0098	0.0020	−0.0154	0.0077
O1_2	0	0.0204	0.0098	0	−0.0174	−0.0155
O2	0	0	0	0	0.0284	0

3.3. Magnetic characterization

The temperature dependence of the magnetic susceptibility within 2–300 K is shown as an inset in Fig. 5. Data appear to have an inverse temperature form typical for paramagnetic behaviour, which is commonly described by Curie–Weiss law:

$$\chi = \frac{N\mu_B^2\mu_{eff}^2}{3k(T-\theta)} = \frac{C}{T-\theta}. \quad (1)$$

Expression (1) contains quantities with their usual abbreviations: N (Avogadro number), μ_B (Bohr magneton), μ_{eff} (effective magnetic moment), k (Boltzmann constant), C (Curie constant), T (temperature in K) and θ (Curie–Weiss temperature, commonly assumed as an indication of the type and strength of the exchange interactions present in a material).

This normally transfers to a simple linear $\chi^{-1}(T)$ dependence, but an inspection of the inverse susceptibility plot (Fig. 5) reveals a sharp deviation from Curie–Weiss law. This is caused by a crystal field influence that is – apart from Sm and Eu – usually observed for the vast majority of rare-earth ions

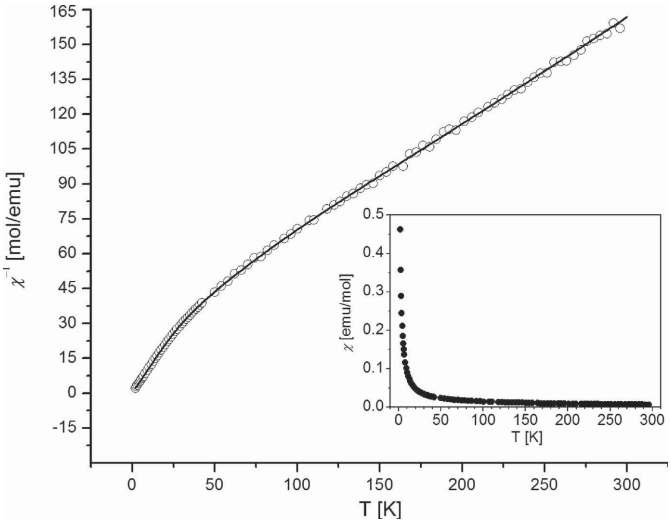

Figure 5
The inverse susceptibility for the $K_3YbSi_2O_7$ sample over the temperature range up to 300 K. The dots represent experimental points, while the full line represents the fitted curve. The temperature dependence of the magnetic susceptibility is shown as an inset.

when studied at a very low temperature ($\sim 10^1$ K). In the present case, the deviation can be detected up to 100 K, which suggests the existence of a very strong crystal field around the symmetrically independent Yb^{3+} ion in $K_3YbSi_2O_7$.

To fully describe the susceptibility data, it is thus necessary to consider the crystal field splitting of the Yb^{3+} ground manifold $^2F_{7/2}$, which is an eightfold degenerated level. The first excited manifold $^2F_{5/2}$ is 10000 cm^{-1} above $^2F_{7/2}$ ($\sim$14400 K), so it does not contribute to the magnetic properties within the measured temperature range. In both $K_3YbSi_2O_7$ polymorphs, the Yb^{3+} ion is in the centre of an oxygen octahedron, with only slight differences between two phases concerning the Yb–O distances. In both cases, the site local symmetry is lower than cubic, so $^2F_{7/2}$ splits into four levels with twofold degeneracy (Kramer's doublets).

In order to describe the susceptibility within the whole temperature range, one has to account for the thermal population of Kramer's doublets, so the molar susceptibility of $K_3YbSi_2O_7$ is described by the following expression (Mitric *et al.*, 1997):

$$\chi = \frac{Ng_J^2\mu_B^2}{k(T-\theta)} \frac{\sum_i M_{ieff}^2 \exp\left(-\frac{E_i}{kT}\right)}{\sum_i \exp\left(-\frac{E_i}{kT}\right)}, (i = 0, 1, 2 \text{ and } 3), \quad (2)$$

where g_J represents the Landé splitting factor. Compared to (1), equation (2) contains two additional elements: M_{ieff} (an 'effective magnetic number', assigned to its corresponding Kramer's doublet) and E_i (the energy gap between the ground ($i = 0$) and ith excited doublet). Effective magnetic numbers, M_{ieff}, quantify the Zeeman splitting of each individual doublet, in the same manner as the magnetic quantum numbers M_J do for the Zeeman splitting of a free ion ground level.

In most cases, fitting of the equation (2) to experimental data can be difficult, since it assumes a large number of free parameters to be fitted to a relatively flat curve. Even in the present case of only four levels, there are still seven parameters to be fitted to the $\chi^{-1}(T)$ data, which are linear over more than 60% of the measured temperature interval. In addition, only those crystal field levels that are significantly populated within the considered temperature interval can be 'observable' by using equation (2). Thus, its successful application is limited by the overall number of crystal field levels (number of parameters), the overall width of the splitting and the temperature range of the measurement.

Fortunately, some information can be deduced in a simpler way. The linear part of $\chi^{-1}(T)$ below 10 K corresponds to the population of the ground doublet exclusively. In such case, expression (2) is reduced to:

$$\chi = \frac{Ng_J^2\mu_B^2 M_{0eff}^2}{k(T-\theta)}. \quad (3)$$

Fitting this equation to the $\chi^{-1}(T)$ data between 2 K and 10 K allows the determination of M_{0eff} and the Curie–Weiss temperature θ. Their values are presented in Table 11. Determination of θ in this manner is particularly advantageous since it corresponds solely to exchange interactions. The obtained value of $\theta = -0.015$ K shows that exchange interactions are practically negligible in $K_3YbSi_2O_7$. It is interesting to note that, otherwise commonly performed, fitting of the Curie–Weiss law (1) to $\chi^{-1}(T)$ data above 150 K gives $\theta = -56$ K. This clearly illustrates how much the θ value can be biased by the crystal field influence when extracted from high-temperature fitting to the Curie–Weiss law.

Table 11
Effective magnetic numbers and positions of the crystal field levels of the symmetrically independent Yb^{3+} ion in $K_3YbSi_2O_7$.

M_{0eff}^2	M_{1eff}^2	M_{2eff}^2	E_1/k (K)	E_2/k (K)	θ (K)	θ (K)†
1.904 (3)	4.4 (3)	7.1 (2)	82 (4)	253 (19)	−0.015 (3)	−56 (1)

† Obtained from Curie–Weiss law within the 150–300 K range.

Using (2), it was possible to obtain the positions and effective magnetic numbers for the three lowest Kramer's doublets. With the exception of M_{0eff}, which was deduced from (3), four parameters (corresponding to the effective magnetic numbers and positions of the first and second excited doublets) were refined. Their values are summarized in Table 11. The attempt to refine the same parameters for the highest doublet was unsuccessful (resulting in unacceptably high standard deviations), which points to an insufficient influence (population) of that level within the measured temperature range.

The phase transition between the β'- and β-$K_3YbSi_2O_7$ polymorphs has no apparent influence on the magnetic properties of $K_3YbSi_2O_7$ around the transition temperature of about 210 K. An obvious reason may due to the fact that both phases are magnetically equivalent (paramagnetic), but also because that the β'-$K_3YbSi_2O_7 \leftrightarrow \beta$-$K_3YbSi_2O_7$ transition occurs at temperatures significantly above 100 K. In that region, dominating doublets are already populated, with their population being almost invariable with temperature [hence the $\sim 1/T$ susceptibility dependence, *i.e.* linearity in $\chi^{-1}(T)$]. It is reasonable, therefore, to assume that a slight level repositioning (if any) due to the modest variation of the Yb—O distances, will not introduce notable changes in the magnetic behaviour above 100 K.

However, it is also reasonable to assume that, to some (unknown) extent, the parameter values listed in Table 11 should be regarded as an 'average' between the two phases since the $\chi^{-1}(T)$ data were fitted as one, continuous curve (with the exception of M_{0eff} that exclusively corresponds to β'-$K_3YbSi_2O_7$).

4. Conclusion

Besides the already known hexagonal structure of α-$K_3YbSi_2O_7$, two new polymorphic modifications – β-$K_3YbSi_2O_7$ and β'-$K_3YbSi_2O_7$ were obtained and described. From the SCXRD data collections between 93 K and 298 K it is evident that β-$K_3YbSi_2O_7$ reversibly transformed into β'-$K_3YbSi_2O_7$ at $\simeq$ 210 K. The transition is due to tilting of SiO_4 tetrahedra resulting in a decrease of the Si—O—Si angle from 180° (dictated by symmetry in space group $P6_3/mmc$) to

$\simeq 164^{\circ}$. This induces differences in the orientation of the SiO_4 tetrahedra and the coordination of the potassium atoms, a shortening of the *c* axis and consequently decreasing unit-cell volume. The influence of the transition on the *a* axis is less pronounced. All this suggests a displacive-type phase transition, which could be adequately described using basic concepts of mode analysis. The very small change in the geometry of the YbO_6 octahedron with temperature is in accordance with the results of magnetic measurements. In addition, positions of the three lowest Kramer's levels of Yb^{3+} ion in $K_3YbSi_2O_7$ are deduced by magnetization analysis, which can be of interest concerning luminescent properties of both polymorphs.

Funding information

The following funding is acknowledged: Ministry of Education, Science and Technological Development of the Republic of Serbia (contract No. 451-03-09/2021-14/200126); Ministry of Education, Science and Technological Development of the Republic of Serbia & Austria Federal Ministry of Education, Science and Research (project No. 451-03-02141/2017-09/14; WTZ project No. SRB 14/2018); Slovenian Research Agency (grant No. P2-0348); Czech Science Foundation (project No. 18-10504S).

References

Alvarez, S. (2013). *Dalton Trans.* **42**, 8617–8636.
Ananias, D., Paz, F. A. A., Yufit, D. S., Carlos, L. D. & Rocha, J. (2015). *J. Am. Chem. Soc.* **137**, 3051–3058.
Brese, N. E. & O'Keeffe, M. (1991). *Acta Cryst.* B**47**, 192–197.
Brown, I. D. & Altermatt, D. (1985). *Acta Cryst.* B**41**, 244–247.
Busch, G., Kaldis, E., Verreault, R. & Felsche, J. (1970). *Mater. Res. Bull.* **5**, 9–17.
Clark, R. C. & Reid, J. S. (1995). *Acta Cryst.* A**51**, 887–897.
Dabić, P., Nikolić, M. G., Kovač, S. & Kremenović, A. (2019). *Acta Cryst.* C**75**, 1417–1423.
Felsche, J. (1973). *The Crystal Chemistry of the Rare-Earth Silicates.* In *Rare Earths. Structure and Bonding*, Vol. 13. Berlin, Heidelberg: Springer.
Figueiredo, B. R., Valente, A. A., Lin, Z. & Silva, C. M. (2016). *Microporous Mesoporous Mater.* **234**, 73–97.
Funk, C., Köhler, J., Lazar, I., Kajewski, D., Roleder, K., Nuss, J., Bussmann-Holder, A., Bamberger, H., van Slageren, J., Enseling, D., Jüstel, T. & Schleid, T. (2018). *Cryst. Growth Des.* **18**, 6316–6325.
Gao, Y., Shen, H., Cao, J., Li, D. & Yang, D. (2019). *Opt. Mater. Expr.* **9**, 4339–4347.
Giacovazzo, C., Monaco, H. L., Viterbo, D., Scordari, F., Gilli, G., Zanotti, G. & Catti, M. (1992). *Fundamentals of Crystallography*, edited by C. Giacovazzo, pp. 387–388. New York: IUCr/Oxford University Press.
Gibbs, G. V., Meagher, E. P., Newton, M. D. & Swanson, D. K. (1981). In *Structure and Bonding of Crystals*, Vol. 1, edited by M. O'Keeffe & A. Navrotsky, pp. 195–225. New York: Academic Press.
Hu, W., Zhang, J., Nian, H. & Wang, J. (2019). *J. Am. Ceram. Soc.* **102**, 490–497.
Latshaw, A. M., Chance, W. M., Trenor, N., Morrison, G., Smith, M. D., Yeon, J., Williams, D. E. & zur Loye, H.-C. (2015*a*). *CrystEngComm*, **17**, 4691–4698.
Latshaw, A. M., Hughey, K. D., Smith, M. D., Yeon, J. & Zur Loye, H.-C. (2015*b*). *Inorg. Chem.* **54**, 876–884.
Latshaw, A. M., Morrison, G., Loye, K. D., Myers, A. R., Smith, M. D. & zur Loye, H. (2016*c*). *CrystEngComm*, **18**, 2294–2302.
Latshaw, A. M., Wilkins, B. O., Chance, W. M., Smith, M. D. & zur Loye, H.-C. (2016*a*). *Solid State Sci.* **51**, 59–65.
Latshaw, A. M., Wilkins, B. O., Hughey, K. D., Yeon, J., Williams, D. E., Tran, T. T., Halasyamani, P. S. & zur Loye, H.-C. (2015*c*). *CrystEngComm*, **17**, 4654–4661.
Latshaw, A. M., Yeon, J., Smith, M. D. & zur Loye, H.-C. (2016*b*). *J. Solid State Chem.* **235**, 100–106.
Lazic, B., Kahlenberg, V., Kaindl, R. & Kremenović, A. (2009). *Solid State Sci.* **11**, 77–84.
Liebau, F. (1985). *Structural Chemistry of Silicates: Structure Bonding and Classification*, p. 347 Berlin, Heidelberg: Springer-Verlag.
Meagher, E. P., Tossell, J. A. & Gibbs, G. V. (1979). *Phys. Chem. Miner.* **4**, 11–21.
Mitric, M., Antic, B., Balanda, M., Rodic, D. & Napijalo, M. L. (1997). *J. Phys. Condens. Matter*, **9**, 4103–4111.
Momma, K. & Izumi, F. (2011). *J. Appl. Cryst.* **44**, 1272–1276.
Morrison, G., Latshaw, A. M., Spagnuolo, N. R. & Zur Loye, H.-C. (2017). *J. Am. Chem. Soc.* **139**, 14743–14748.
O'Keeffe, M. & Hyde, B. G. (1978). *Acta Cryst.* B**34**, 27–32.
O'Keeffe, M. & Hyde, B. G. (1996). *Crystal Structures I. Patterns and Symmetry.* Washington D. C.: Mineralogical Society of America.
Orobengoa, D., Capillas, C., Aroyo, M. I. & Perez-Mato, J. M. (2009). *J. Appl. Cryst.* **42**, 820–833.
Palatinus, L. & Chapuis, G. (2007). *J. Appl. Cryst.* **40**, 786–790.
Peterse, W. J. A. M. & Palm, J. H. (1966). *Acta Cryst.* **20**, 147–150.
Petříček, V., Dušek, M. & Palatinus, L. (2014). *Z. Kristallogr. Cryst. Mater.* **229**, 345–352.
Petříček, V., Dušek, M. & Plášil, J. (2016). *Z. Kristallogr. Cryst. Mater.* **231**, 583–599.
Rigaku Oxford Diffraction (2014). *CrysAlisPro*, version 1.171.38.43. Rigaku Corporation, Oxford, UK.
Shannon, R. D. (1976). *Acta Cryst.* A**32**, 751–767.
Sheldrick, G. M. (2015). *Acta Cryst.* C**71**, 3–8.
Sun, Z., Li, M. & Zhou, Y. (2014). *Int. Mater. Rev.* **59**, 357–383.
Vidican, I., Smith, M. & zur Loye, H.-C. (2003). *J. Solid State Chem.* **170**, 203–210.
Voronko, Y. K., Sobol, A. A., Shukshin, V. E. & Gerasymov, I. (2015). *Inorg. Mater.* **51**, 1039–1046.
Wills, A. S. (2010). *VaList.* Program available from http://fermat.chem.ucl.ac.uk/spaces/willsgroup/software/valist-bond-valence-calculations-listing/.
Zhang, F. X., Lang, M., Zhang, J. M., Cheng, Z. Q., Liu, Z. X., Lian, J. & Ewing, R. C. (2012). *Phys. Rev. B*, **85**, 214116.
Zhang, F. X., Xiao, H. Y., Lang, M., Zhang, J. M., Zhang, Y., Weber, W. J. & Ewing, R. C. (2013). *Phys. Chem. Miner.* **40**, 817–825.